Journal of Materials Processing Tech. 327 (2024) 118354

Contents lists available at ScienceDirect

Journal of Materials Processing Tech.

journal homepage: www.elsevier.com/locate/jmatprotec

Additively manufactured β-Ti5553 with laser powder bed fusion: Microstructures and mechanical properties of bulk and lattice parts

Margaret Wu [a], Marissa Linne [a], Jean-Baptiste Forien [a], Nathan R. Barton [a], Jianchao Ye [a], Kavan Hazeli [b], Aurelien Perron [a], Kaila Bertsch [a], Y. Morris Wang [c], Thomas Voisin [a,*]

[a] Lawrence Livermore National Laboratory, 7000 East Avenue, Livermore, CA 94550, USA
[b] University of Arizona, 1200 E University Blvd, Tucson, AZ 85721, USA
[c] University of California Los Angeles, 410 Westwood Plaza, Los Angeles, CA 90095, USA

ARTICLE INFO

Associate Editor: Dragos Axinte

Keywords:
Ti5553
Additive manufacturing
Lattices
Electron microscopy
Digital image correlation

ABSTRACT

Ti5553 (Ti-5Al-5Mo-5V-3Cr wt%) is a titanium alloy widely used for its high strength-to-weight ratio and good formability at elevated temperatures. Unlike Ti-6Al-4V, Ti5553 does not undergo martensitic transformation, preventing cracking of brittle martensite upon rapid cooling. This makes it a strong candidate for additive manufacturing (AM), particularly laser powder bed fusion (L-PBF). L-PBF offers the unique opportunity to make fine lattice structures to reduce component weight. Despite the growing field of AM, there have been limited studies on L-PBF Ti5553 lattices and how their properties differ from the bulk. The present work addresses this knowledge gap by investigating microstructures and properties of L-PBF bulk and lattice parts and the effect of post L-PBF heat treatments. Electron microscopy and mechanical testing show that the high dislocation density formed during L-PBF increases bulk part's yield strength by approximately 100 MPa compared to the conventional alloy. Digital image correlation during compression testing of octet truss lattices reveals a layer-by-layer failure mode. Compared to the bulk, the lattice contains copious ω nanoprecipitation, weaker <001> texture, smaller average grain sizes, and larger content of high-angle grain boundaries. These features elicit differences in Taylor factor distributions for the lattice depending on load direction, underlining challenges in predicting lattice mechanical response based on bulk properties. By examining the processing-structure-property relationships in the bulk and lattice, the present results delineate their microstructural and mechanical differences and establish a benchmark for the future design applications of L-PBF Ti5553.

1. Introduction

Ti5553 (Ti-5Al-5Mo-5V-3Cr wt%) is a metastable body-centered cubic (β) titanium alloy used in structural applications due to its high strength-to-weight ratio and advantageous fracture toughness compared to other Ti-based alloys (Ghosh et al., 2013). Compared to Ti-6Al-4V, Ti5553 has a slightly higher density (4.67 g/cc vs 4.43 g/cc). However, it retains a near-β microstructure after quenching from a lower transus temperature (~840°C), yielding higher formability as well as opportunities to tailor mechanical performance based on thermal history (Cotton et al., 2015; Clement et al., 2007). For example, subsequent annealing within the α (hcp) + β region introduces intragranular precipitates which enhance strength (Shekhar et al., 2015; Kar et al., 2013). Unlike Ti-6Al-4V, Ti5553 does not undergo martensitic transformation upon rapid cooling. This makes Ti5553 easier to process with additive manufacturing (AM) because the absence of brittle α' phase improves the material formability and prevents cracking.

Laser powder bed fusion (L-PBF), an additive manufacturing (AM) technique, involves the layer-by-layer fabrication of complex 3D parts and expedites their deployment since the components can be built on-demand without multi-step assembly. Moreover, L-PBF enables the reduction of component weight due to the fabrication of intricate geometries such as lattices, which are especially valuable for aerospace and automotive applications. However, the realization of L-PBF Ti5553 depends on a comprehensive understanding of the alloy's microstructure, mechanical behavior, and optimal processing window. To date, the literature on bulk L-PBF Ti5553 is scarce and while the significance of the combined effect of topology and microstructure on the optimization and design strategy of lattice structures has been investigated (Hazeli et al., 2019; Babamiri et al., 2022), the characterization of Ti5553

* Corresponding author.
E-mail address: voisin2@llnl.gov (T. Voisin).

https://doi.org/10.1016/j.jmatprotec.2024.118354
Received 2 October 2023; Received in revised form 15 February 2024; Accepted 25 February 2024
Available online 27 February 2024

lattices is almost non-existent. Thus far, microstructures commonly reported for bulk L-PBF Ti5553 are columnar β-phase grains preferentially aligned along their <100> crystallographic directions, parallel to the build direction and subgrain structures (Schwab et al., 2016; Huang et al., 2021). The effect of this <100> texture on the tensile properties in Ti5553 was investigated by Ramachandiran et al. (2023) who concluded that samples printed parallel to the build direction exhibited a higher strength (~846 MPa) compared to samples printed normal to the build direction (~780 MPa) where the development of slip bands oriented ~45° to the build direction (maximum shear stress along {110} planes) led to fracture by pore coalescence. Other recent work on L-PBF Ti5553 has also included Bakhshivash et al. (2019) who examined the effects of varying the volumetric energy density (VED) on bulk Ti5553 and found that a medium VED value of 112 J/mm^3 produced parts that contained the highest density (>99%) and ω phase precipitates. Meanwhile, Yang et al. (2023) extended their research efforts beyond the scope of mechanical characterization to demonstrate the negligible effects of processing and heat treatment variations on the alloy's thermophysical properties.

In terms of optimizing mechanical performance, most studies on additively manufactured Ti5553 have focused on heat-treatments (Carlton et al., 2019; Schwab et al., 2017) within the α + β regime. In particular Bakhshivash et al. (2019) examined the strengthening effects of the α phase in Ti5553 annealed between 500 – 700ºC while others have focused on the laser deposition of a "hybrid" titanium material consisting of α/β Ti-64 and β-Ti5553 microstructures (Zafari et al., 2020; Zafari and Xia, 2019) to enhance mechanical performance. However, compared to the aforementioned studies which explore the mechanical and thermophysical properties of Ti5553 in the as-built and >500ºC annealed conditions, limited characterization has been conducted on nanoprecipitation in L-PBF Ti5553 after low-temperature (300ºC) heat-treatments or explored whether its presence impacts mechanical properties. This analysis is especially relevant for L-PBF parts, which typically undergo post-process annealing to relieve residual stress.

The present work investigates the hierarchical microstructures of L-PBF Ti5553 bulk in the as-built condition after annealing at either high (>600ºC) or low (300ºC) temperatures as well as lattice parts heat-treated at 300°C, by using scanning electron microscopy (SEM), electron backscatter diffraction (EBSD), transmission electron microscopy (TEM), and X-ray computed tomography (CT). The high-temperature anneal, further confirmed by CALPHAD results, introduces micron-sized α-grains in the β matrix which enhance bulk material strength as evidenced by room-temperature tensile tests. Meanwhile, low-temperature aging introduces sparsely distributed α-nanoprecipitates and a uniform distribution of ω phase. Additionally, compression testing coupled with digital image correlation (DIC) was used to investigate the mechanical performance of Ti5553 lattices.

The present study addresses the following research gaps: (1) how do rapid cooling rates inherent to L-PBF affect the presence of the ω phase known to impact mechanical properties of conventionally cast metastable β-Ti alloys (Zheng et al., 2016a)? Insights are pertinent not only to Ti5553 but most body-centered cubic Ti alloys; (2) do dislocation cells, previously observed in LPBF cubic metals and which have been shown to strongly influence mechanical properties (Voisin et al., 2021a), play a similar role in L-PBF Ti5553? (3) How do the small diameter and different orientations of LPBF Ti5553 lattice struts impact their microstructural features such as grain size and texture? By comprehensively investigating the microstructural and mechanical differences between the bulk and lattice, we seek to not only provide a starting framework for the successful post-processing of Ti5553 parts, but also show this material system is relevant to alloys fabricated by similar rapid solidification techniques in addition to additively manufactured lattices whose properties cannot be extrapolated to their bulk counterparts.

2. Methods and materials

All Ti5553 material was made with a SLM-280 L-PBF machine in an argon environment. Octet truss 3×3 lattices were printed using a laser power of 100 W, a scan speed of 800 mm/s, hatch spacing of 120 μm, and layer thickness of 30 μm. Laser scanning direction was rotated by 75° every layer. The reader is referred to (Carlton et al., 2019) for details on the Ti5553 powder used in the current study. Lattice target relative density is 10% and struts are 0.4 mm in diameter and 3 mm long. All lattice parts were heat treated at 300° C for 1 hr. This heat treatment was applied to prevent cracking and deformation of thin struts during removal from the build plate; consequently, Ti5553 lattices were not able to be analyzed in the as-printed state. All heat treatments used in this work were performed in a tube furnace that was vacuumed and backfilled with flowing argon.

Ti5553 bulk plates [50 mm (length) × 10 mm (width) × 50 mm (height)] were printed using a laser power of 100 W, a scan speed of 525 mm/s, a hatch spacing of 120 μm, and a layer thickness of 30 μm. Laser scanning direction was rotated by 75° every layer. Analysis of Ti5553 bulk material was performed on as-printed material, material subjected to a 300°C heat treatment for 1 hour identical to that applied to lattice parts, and on material subject to a heat treatment of 790°C (just below the β-transus) for 2 hours and subsequently aging at 600°C for 6 hours.

High energy X-ray tomography was performed at beamline 8.3.2. of the Advanced Light Source, Berkeley, USA (MacDowell et al., 2012). The monochromator was tuned to deliver an X-ray beam energy of 38 keV on a 50 μm LuAG scintillator placed 69.3 mm away from sample rotation center. Radiography images were collected on a sCMOS PCO-edge detector with 2560 ×2160 pixels array and equipped with 10x lens, resulting in a pixel resolution of 0.65 μm/pixel. A total of 1313 projections were collected around 180-degree range with 1 s exposure. The reconstruction was performed using filtered back projection algorithm provided by the LTTv1.5.2 software package (Champley et al., 2022).

Uniaxial tensile testing on bulk materials was performed with an Instron 4444 tensile tester at the strain rate of 5×10^{-4}/s. Strain was calculated from the displacement in the sample gauge region measured with a LE-01 laser extensometer (Electronic Instrument Research, PA, USA). Tensile specimens were machined from the bulk plates with their loading axes perpendicular to the build direction. Samples had gauge lengths of 6 mm and cross-sections of 2 (width) × 1 (thickness) mm^2. Quasi-static compression testing of lattices was performed using a Materials Testing System load frame (MTS, MN, USA) equipped with a 100 kN load cell. The displacement rate during the tests was set at 1 mm/min, corresponding to strain rates on the order of 1×10^{-3}/s. The Digital Image Correlation (DIC) technique was used to examine strain at the strut level using Vic 2D software (Correlated Solutions, SC, USA). A speckle pattern was applied to one face of the specimens using an airbrush to measure the displacement field and calculate the strain. The speckled face of the specimen was imaged by a PointGrey Grasshopper GS3-U3–64151S5M-C camera (FLIR, Oregon, USA) with a resolution of 2448 × 2048 pixels at 1 frame per second. The required illumination was provided by a Cole-Parmer 41500–50 fiber optic illuminator (IL, USA). Global strain in the lattice structures was calculated from the cross-head displacement recorded by the MTS machine, as extending DIC local strain measurements to global strain has been shown to be inaccurate for AM lattice structures, while cross-head displacement has been shown to be reliable (Hazeli et al., 2019). Compressive stress was calculated using $\sigma = F/Sa$, where σ represents stress, F is the force, and Sa is the cross-sectional areas of the sample.

Metallographic samples for both bulk and lattice samples were prepared for electron backscatter diffraction (EBSD) using standard metallographic techniques. Samples were ground on an automatic polishing system (Allied Met Prep 4) with silicon carbide paper (420, 600 and 800 grit) and then polished with 3 μm diamond paste. The final polishing step was a chemical polish conducted on the automatic

polishing system using a 1:1 solution of 0.25 μm colloidal silica (Struers OP-S) and hydrogen peroxide. EBSD maps were collected from the polished samples using 20 kV accelerating voltage and step size of 0.1–0.5 μm with a ThermoFisher Apreo SEM and EDAX Velocity EBSD camera. Data were collected with TEAM™ EBSD Analysis System and analyzed with OIM Analysis™, both from EDAX. Taylor Factors were calculated using the three different families of slip systems known to potentially be active in bcc crystals: <110>(-111) 12 systems, <211>(-111) 12 systems, <321>(-111) 24 systems.

For TEM analysis, the bulk material was ground into foils ~100 μm in thickness then laser-cut into 3 mm disks. Using a Struers Tenupol twin-jet polisher, the disks were electropolished using a solution of 60% methanol, 35% butanol, and 5% perchloric acid at 15 V and −25°C followed by ion polishing using a Precision Ion Polishing System II (Gatan Inc.). TEM samples made from lattice parts were prepared using focused ion beam (FIB). TEM investigations were conducted in a FEI 80–300 Titan TEM operated at 300 kV. Phase stability of Ti5553 was investigated using the CALPHAD method. CALPHAD is based on Gibbs energy modeling, which involves the selection of appropriate thermodynamic models for the Gibbs energy as functions of pressure, temperature and chemical composition, and the maximum-likelihood estimation of model parameters (Kaufman and Bernstein, 1970; Saunders N, 1998). To do so, critically selected thermochemical and constitutional data are used as input, and the process ultimately leads to an optimized thermodynamic description of the system. In the present study, we use the Thermo-Calc (version 2022b) computational thermodynamic software–to perform equilibrium calculations via Gibbs energy minimization–in combination with the encrypted TCTI2 database (which contains the aforementioned optimized model parameters for Ti-rich alloys).

3. Results

3.1. Microstructure and mechanical properties of bulk as-printed Ti5553

The as-built Ti5553 microstructure is highly textured and the elongated grain morphology resembles previous additively manufactured titanium alloys (Liu et al., 2019; Hernandez et al., 2013). Fig. 1a is an inverse pole figure (IPF) map image of the specimen surface viewed perpendicular to the build direction (BD) showing an average grain size of 34.2 μm (Supplementary Information - Fig. S1) and a strong <001> texture as illustrated by the corresponding pole figures. This strong texture is due to the alignment of the maximum heat flow direction with the preferred <001> growth direction for cubic crystals during solidification (DebRoy et al., 2018). When viewed parallel to the build direction, the sample contains features of epitaxial growth such as columnar β grains (Fig. 1b,e) with an average grain size of 107.6 μm (Supplementary Information - Fig. S2a) which are oriented along the BD while maintaining texture across melt pool boundaries (Fig. 1c). Additionally, the percentage of low angle grain boundaries (<10°) is approximately 70% (Supplementary Information - Fig. S2b). The higher magnification image from the inset of Fig. 1d reveals rapid solidification cellular/dendritic structures similar to that observed in other AM metals (Zhong et al., 2016; Wang et al., 2018).

However, it should be noted that interdendritic regions did not retain dislocations to form networks usually observed in L-PBF cubic-structure metals (Bertsch et al., 2020; Voisin et al., 2021b). Instead, when the same specimen is imaged under bright-field (BF) TEM, only randomly distributed dislocation tangles are observed (Fig. 2a). Moreover, interdendritic regions contain minimal elemental partitioning as shown by STEM high angle annular dark-field (HAADF) imaging with corresponding STEM-EDS maps (Fig. 2b). Previous work on direct laser deposited Ti5553 containing larger substructure sizes (~14 μm) showed <1 wt% difference in Mo and Cr content between the cellular-dendritic

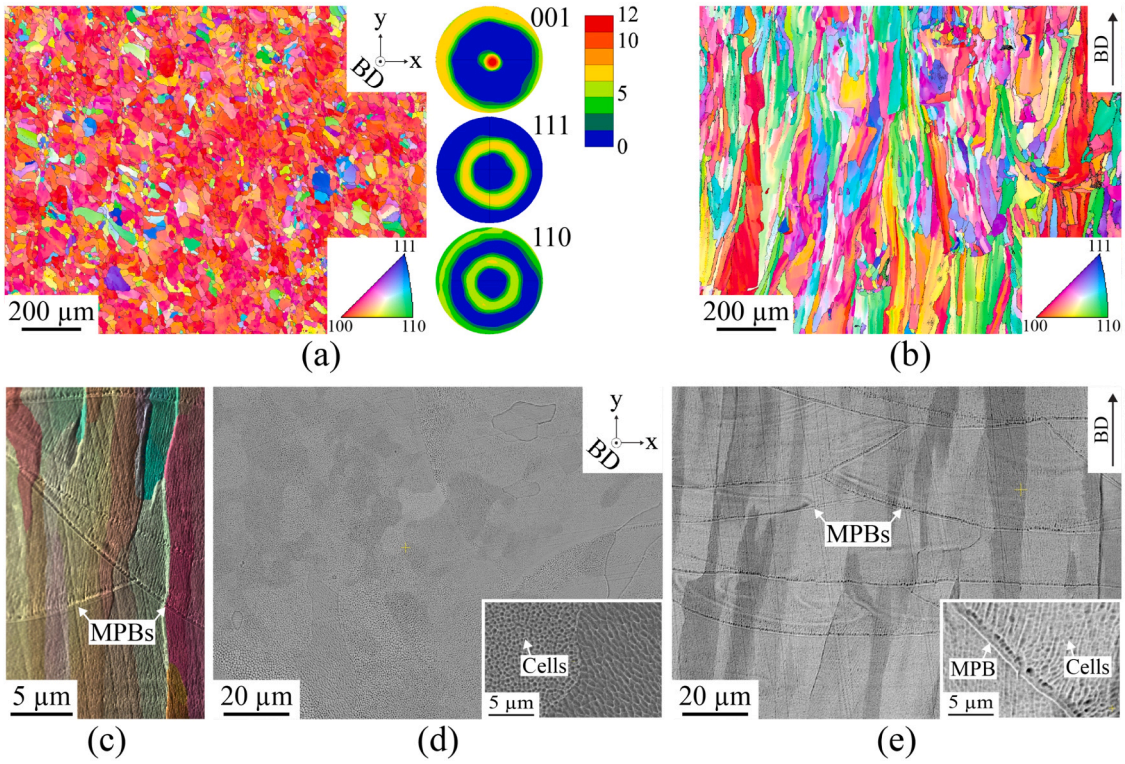

Fig. 1. : Microstructure of the as-printed SLM-280 Ti5553 by SEM. (a) EBSD IPF map and corresponding pole figures of a cross section perpendicular to the build direction; (b) EBSD IPF map of a surface parallel to the build direction; (c) overlayed EBSD IPF with a BSE image; (d) and (e) BSE SEM images of etched surfaces perpendicular and parallel to the build direction, respectively. MPB stands for Melt Pool Boundary.

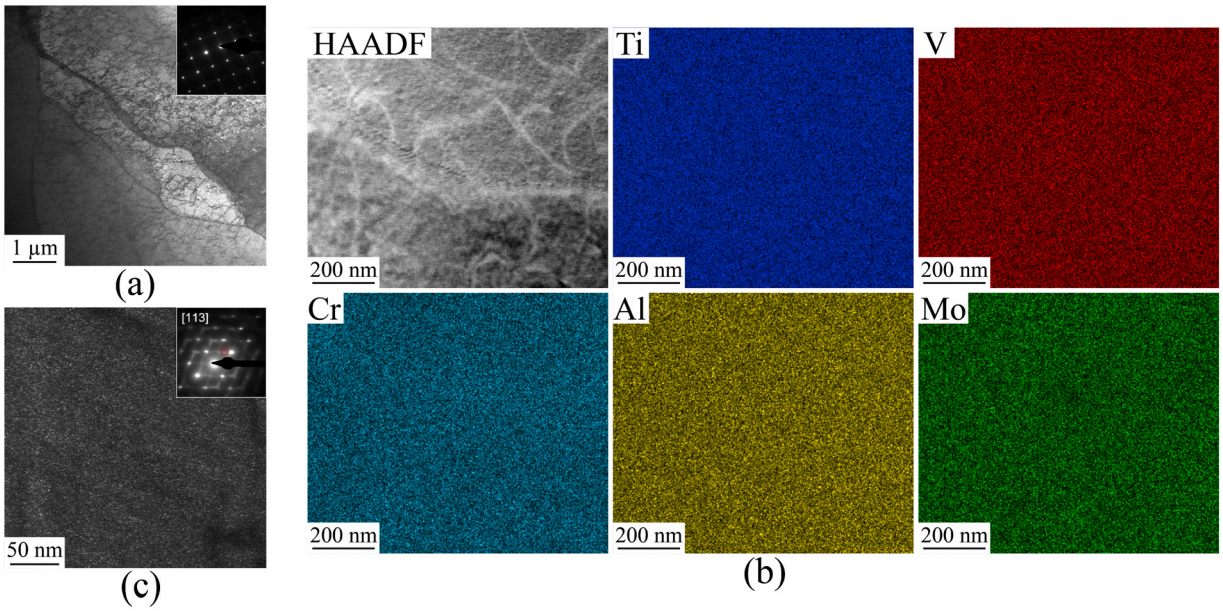

Fig. 2. : Microstructure of the as-printed SLM-280 Ti5553 by TEM. (a) BF-TEM image of dislocation tangles; (b) STEM-HAADF and STEM-EDS maps. (c) DF-TEM images with the corresponding [113] SADP as inset. The red circle highlights the diffraction spot used to reveal the ω-phase.

structure interiors compared to boundaries (Sharma et al., 2021). However, the minimal elemental segregation within these structures still enables preferential etching as observed in the BSE SEM image at the inset of Fig. 1d. Fig. 2c shows the as-printed bulk material imaged via DF-TEM. The corresponding [113] selected area diffraction pattern (SADP) at the inset contains diffuse streaking along $<112>_{\beta}$ and faint spots at the 1/3 and 2/3$\{112\}_{\beta}$ positions characteristic of the athermal hexagonal ω phase (Jones et al., 2009; Williams et al., 1973). The reflection circled in red was used to image the nanoscale ω precipitates in the corresponding DF-TEM image.

The engineering stress-strain curve for Ti5553 in the as-printed condition is reported in Fig. 3. The yield strength, ultimate tensile strength, and elongation to failure for the as-printed material are 903 ± 8 MPa, 915 ± 10 MPa, and 15 ± 1%, respectively. As previously seen for Ti5553, work hardening is minimal which leads to a low uniform elongation (UE) value <3%. Additionally, a prolonged softening post-yield is observed for the as-built material which is characteristic of β titanium alloys (Min et al., 2015; Agarwal et al., 2008).

3.2. *Microstructure and mechanical properties of Ti5553 lattice*

Due to the significantly smaller size of lattice ligaments and nodes compared to bulk material, and the fact that melt pools in lattice parts are surrounded by less previously-built material for heat conduction, lattices may experience a different cooling rate than bulk samples. This can affect their microstructure and corresponding mechanical properties. Additionally, it is important to note that all lattice parts were annealed at 300°C before removal from build plates to prevent cracking and warping of the thin struts due to residual stresses during the removal process.

Lattice parts are dense with significant surface roughness. Fig. 4 is a snapshot of an X-ray computed tomography (CT). CT and SEM did not reveal porosity in the as-printed lattice. However, high surface roughness is observed due to melt pool instability and partially melted particles. Furthermore, EBSD IPF maps for the ligaments oriented 45° and

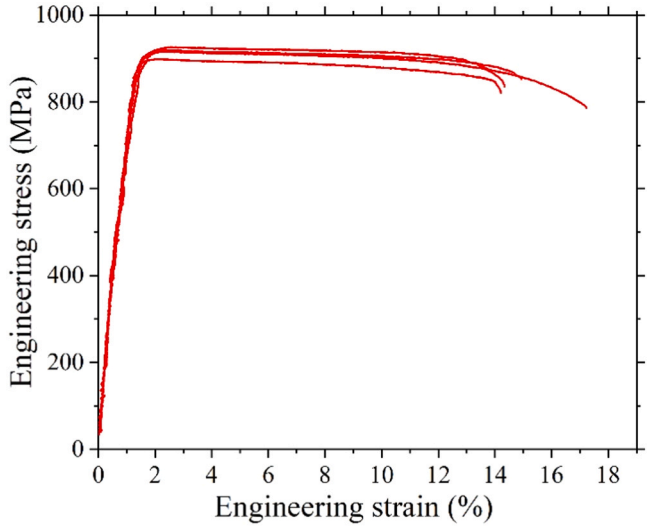

Fig. 3. Tensile properties of as-printed materials tested at room temperature and quasistatic strain rate.

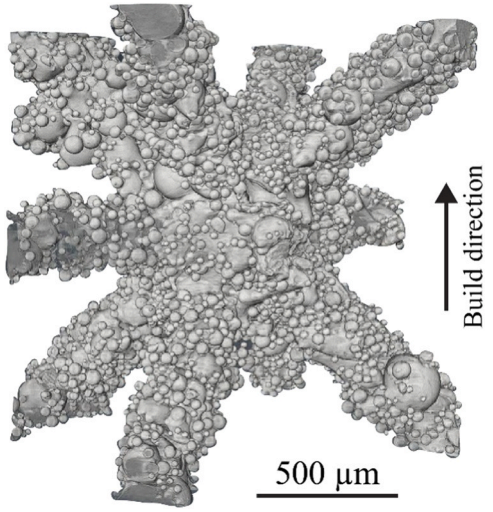

Fig. 4. X-ray CT of the lattice structure containing partially melted powder particles.

90° (Fig. 5) from the BD display primarily β phase microstructure with local variation in grain size and shape, i.e. grains within the feedstock powder particles from the surrounding powder bed are partially melted by the laser source and fuse onto the strut surfaces during L-PBF. These "satellite particles" appear more equiaxed compared to the elongated grains at the strut interior and are especially prevalent at the bottom of the 90° ligaments, which was supported by only the powder bed. Moreover, the corresponding EBSD pole figures indicate a weaker texture than that of the bulk. Note that the <001> texture along the BD is observed in the 90°-oriented ligament but not in the 45°-oriented one. Instead, the <001> texture is closer to the direction of elongation of the ligament, indicative of a change in heat flow direction during solidification. The average grain sizes for the 45° and 90°-ligaments of 62 μm and 57.3 μm, respectively (Supplementary Information - Fig. S2a), are smaller than for the bulk (107.6 μm when microstructure is similarly viewed with the BD within the plane). However, compared to the bulk, ligaments of both orientations contain a lower LAGB content and larger average grain boundary misorientation, as illustrated by the peak in grain boundaries observed with near-30° misorientation for the 90° strut in Fig. S2b (Supplementary Information). The substantial variation in lattice strut grain shape and size is further seen in the strut cross-sections (Fig. 5).

Metastable phases were also observed in both the struts and the nodes (Fig. 6). The inset in Fig. 6a is a [012] SADP of the 45°-oriented lattice strut. As previously noted, the characteristic diffraction spots at the $1/3\{112\}_\beta$ and $2/3\{112\}_\beta$ positions indicate the presence of the ω phase. Moreover, the corresponding DF-TEM image (Fig. 6a) was acquired using the $1/3\{112\}\beta$ reflection circled in red, which consequently highlights the ellipsoidal ω nanoprecipitates. Similarly, for the 90°-oriented strut, the extra reflection spots at 1/3 and $2/3\{112\}_\beta$ locations in the [113] SADP inset confirm the presence of ω-phase particles in the DF-TEM image (Fig. 6b). Similar to the struts, the lattice node (Fig. 6c) also displays characteristic ω diffraction spots as evidenced in the [012] SADP and corresponding DF image. The presence of the ω phase is expected since the lattice was aged at 300°C, which is below the ω solvus of ~450°C (Jones et al., 2009; Song et al., 2020) and its uniform distribution within grains is apparent in Fig. S3 (Supplementary Information). In addition to ω, another minor phase is observed. Alongside ω, the martensitic α" phase can form in quenched (Zheng et al., 2016b) or aged (Settefrati et al., 2013; Paiotti Marcondes Guimarães et al., 2020) metastable β alloys. Accordingly, Fig. 6 contains [001] SADPs for the (d) 45°-oriented and (e) 90°-oriented struts as well as (f) node, which all display distinct reflections at the ½β positions. These extra spots are characteristic of the orthorhombic α" martensite and form by shearing of atoms on every other set of $\{110\}_\beta$ planes (Banerjee and Williams, 2013). In contrast, the ω phase reflections completely overlap with the β reflections under the [001] zone axis (Alphy et al., 2017). Therefore, the corresponding DF TEM images using the reflections circled in red confirm the presence of α" particles. Finally, as observed for the bulk annealed at 300ºC for 1 h, a sparse distribution of α precipitates were observed in the 45º and 90º-ligaments in Fig. 6 g, h, respectively.

3.3. *Effect of 300°C anneal and ω phase on bulk microstructure and mechanical properties*

In accordance with previous residual stress relief studies (Carlton et al., 2019), Ti5553 bulk parts were annealed at 300°C for 1 h. The effects of this heat-treatment on the nanoprecipitation commonly reported for β-titanium alloys (Lütjering et al., 2007) were then analyzed. In particular, the decomposition of β into $\omega_{athermal}$ has been widely documented in quenched β-titanium alloys and involves the shearing of the $\{111\}_\beta$ planes along the <111> direction (Zheng et al., 2016c; Alam, 2014). The additional 1/3 and $2/3\{112\}_\beta$ reflections become more distinct after annealing at 300ºC for 1 h (Fig. 7a). The encircled red reflection was used to record these coarser isothermal ω nanoprecipitates, which form when aging within the 200–500ºC temperature range (Panza-Giosa, 2009) and unlike $\omega_{athermal}$, involve the rejection of Al and enrichment of Ti (Nag et al., 2009). Additionally, Fig. 7b contains the DF-TEM image of the 300ºC annealed sample obtained using the [012] zone axis. One of the extra reflections at $1/2\{112\}_\beta$ indicates the hexagonal close-packed α phase (Wain et al., 2010) and the spot circled in red highlights the needle-shaped α nanoprecipitates. The engineering stress-strain tensile curve for the bulk material annealed at 300°C for 1 h

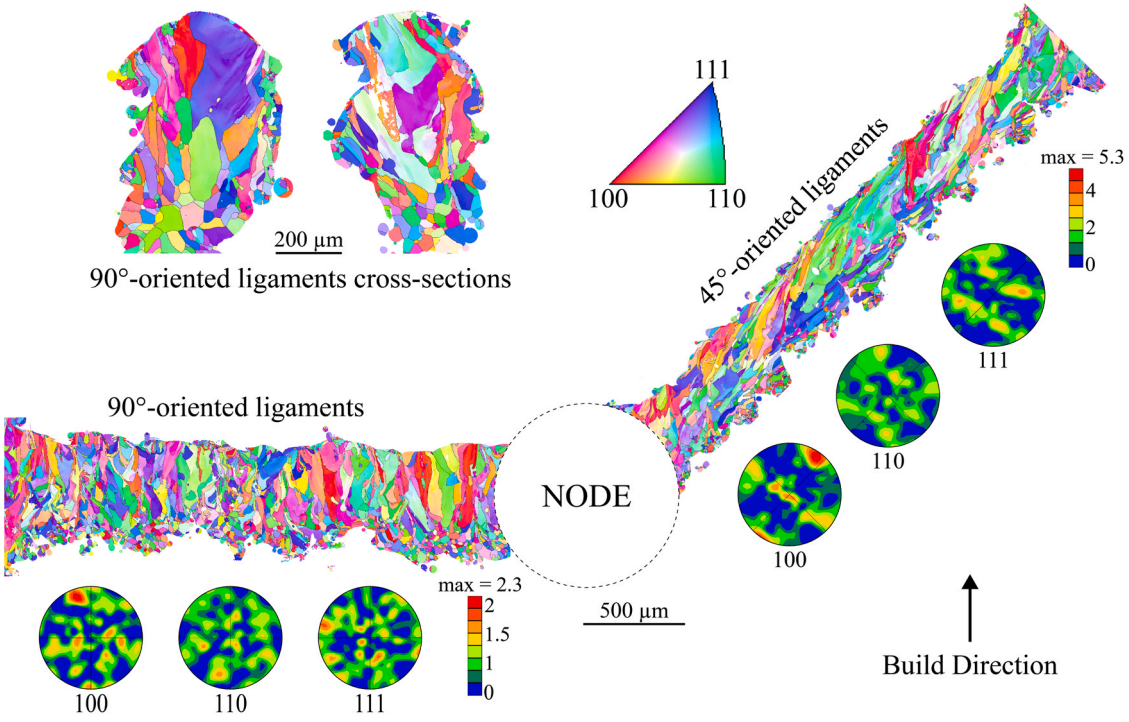

Fig. 5. Microstructure of Ti5553 lattice ligaments. 45° and 90°-oriented ligaments are characterized by SEM/EBSD.

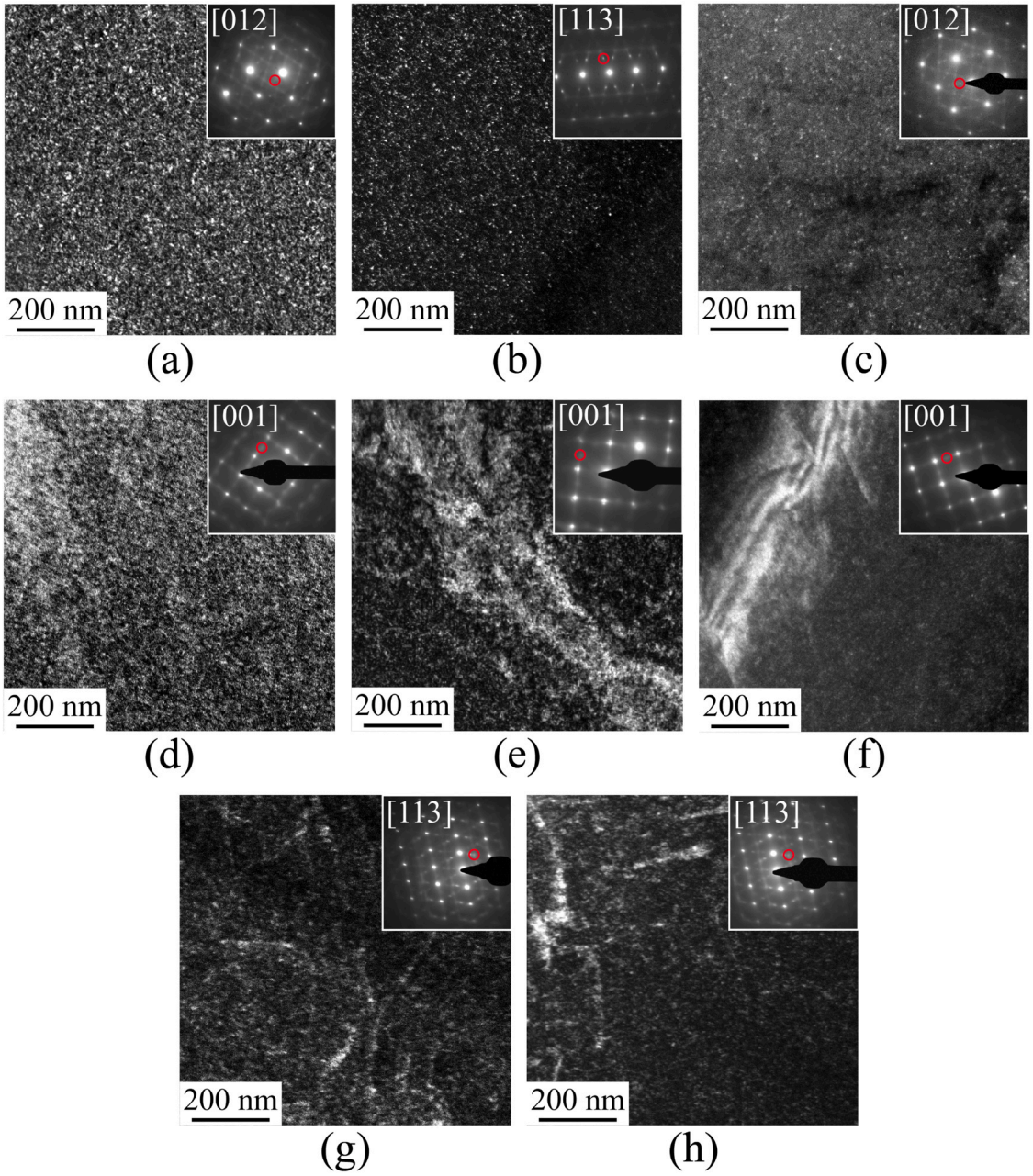

Fig. 6. ω nanoprecipitates in 300°C annealed Ti5553 lattices seen by DF-TEM. Images show ω nanoprecipitates in the struts oriented (a) 45° and (b) 90° from the BD and (c) node. DF-TEM images of the (d) 45°-oriented strut, (e) 90°-oriented strut, and (f) node indicate presence of α" phase. DF-TEM micrographs for the (g) 45° and (h) 90° ligaments contain α precipitates. The circled red reflections in SADPs (insets) were used to generate the DF images.

is seen in Fig. 7a (blue curve). After annealing at 300ºC for 1 h, the yield strength decreases to 848 ± 11 MPa compared to the as-built material (red curve). Also, the 300ºC annealed samples demonstrate a yield drop during plastic deformation comprised of an upper yield point of 849 ± 11 MPa followed by prolonged softening and an elongation to failure (ETF) of 19 ± 2%.

3.4. Mechanical properties of Ti5553 lattice

To gain insight into the deformation mechanisms and damage evolution of the Ti5553 octet lattice structure as well as its individual struts, digital image correlation (DIC) was used during quasistatic compression testing. The octet lattice-truss is a stretch-dominated structure according to Maxwell's instability criteria, i.e. the deformation behavior is dictated by its struts loaded in tension or compression. The octet-truss can fail either through plastic yielding or elastic buckling (D. V et al., 2001). As shown by Movie 1 and the corresponding snapshots of the DIC strain maps (Fig. 8a), at the initial stages of testing, lattice struts oriented diagonal to the build direction are in compression and first show increased strain values (Fig. 8b(1,2)). Localized failure of struts in tension is then initiated due to a load transfer from the diagonal struts that buckle (Fig. 8a(2,3) – red circle marks a broken tension strut). Previous studies have investigated the role of defects such as pores and partially melted powder particles (Carlton et al., 2022) and microstructure (Hazeli et al., 2022) on the elastic buckling of diagonal struts and collapse mechanisms. As seen in the X-ray CT image (Fig. 4), high surface roughness caused by partially fused powder particles may have provided crack initiation sites. The corresponding stress-strain curve in Fig. 8b demonstrates the progressive crushing behavior of the lattice. The layer-by-layer collapse is seen in the DIC video and manifests as a

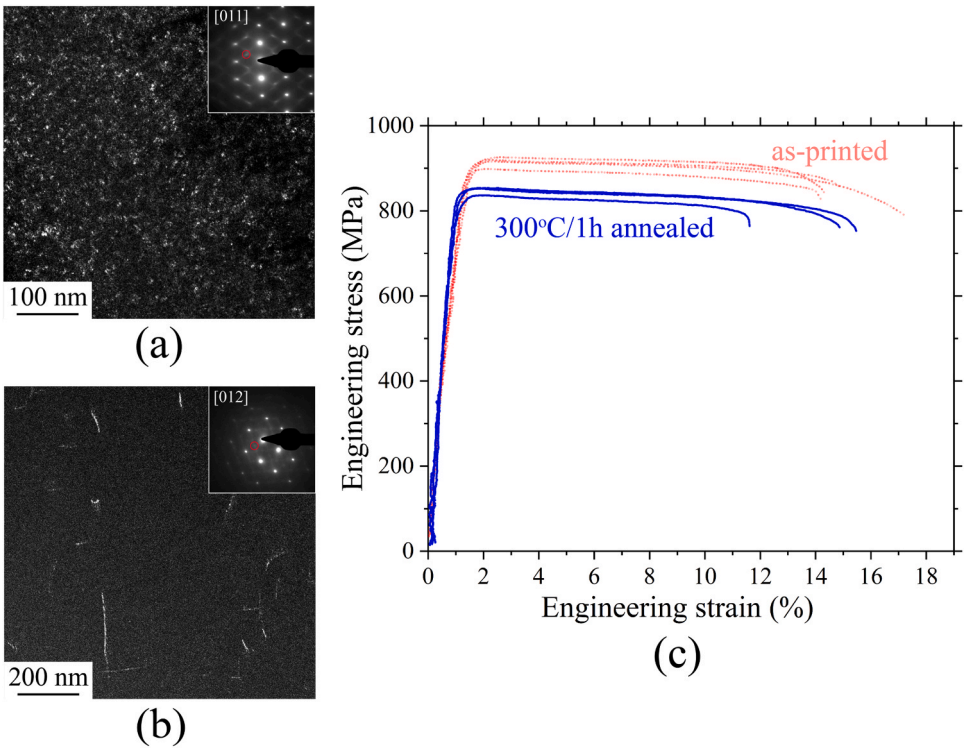

Fig. 7. Effect of precipitates in the 300 °C/1 h annealed material. (a) and (b) DF-TEM images of ω and α precipitates, respectively. Insets are the corresponding SADPs. The red circles on the insets highlight the diffraction spots used to reveal the precipitates. (c) Tensile curves of the annealed material (blue) compared to the as-printed material (transparent red).

multi-peak response within the plateau regime wherein diagonal struts in each layer uniformly compress (Fig. 8a(5,7)) before buckling and collapsing (Fig. 8a(3,6)), resulting in a drop in stress. Densification begins above an engineering compression strain of 50% and is seen as a sharp rise in stress during the final phase of loading, from 55% to 65% strain (Fig. 8a(8)).

Supplementary material related to this article can be found online at doi:10.1016/j.jmatprotec.2024.118354.

3.5. *Microstructure and mechanical properties of α+β annealed Ti5553 bulk*

Improving material strength by introducing the hcp α-phase in metastable β titanium alloys is a common industrial practice (Paiotti Marcondes Guimarães et al., 2020; Banerjee and Williams, 2013). Here, we use a well-established process consisting of heat treating the as-built material at 790°C (just below the β-transus) for 2 hours to tailor the amount of the primary α phase (α_p) and subsequently aging at 600°C for 6 hours to introduce fine secondary precipitates (α_s) that control material strength (Zhang et al., 2018). The effect of this heat treatment on the microstructure is presented in Fig. 9. As expected, the resulting microstructure in Fig. 9a contains the dark-contrast α-phase distributed along the grain boundaries and homogeneously dispersed within the β matrix. The former is associated with α_p and its presence dictates the amount of β stabilizing elements in the retained matrix and therefore the subsequent precipitation of needle-shaped α_s. The EBSD phase map of the annealed material (Fig. 9b) indicates the volume fractions of the β and α phases are 31% and 69%, respectively. As evidenced in Fig. 9c, the former β grain boundaries are only semi-continuously covered by the α-phase, which is crucial for preserving ductility and moreover, can be controlled by careful selection of the α+β solution treatment temperature (Liu et al., 2014).

To confirm the absence of ω phase in the β phase and changes in dislocation content after the high-temperature heat treatment, TEM studies were conducted (Fig. 10). The annealed Ti5553 material is shown in the BF TEM image of Fig. 10a, which displays dark α-particles embedded in the lighter β-matrix. The inset contains the [5143] SADP recorded from the α-grain used to generate the corresponding dark field (DF) TEM image (Fig. 10b) where the previously dark-colored α grains now appear bright. Similarly, the BF TEM image (Fig. 10c) shows the same region using the [012] SADP of the β-phase matrix located at the inset. As can be seen on the SADP, there is no diffraction spot coming from the ω phase. The corresponding DF TEM (Fig. 10d) shows most dislocations that were present in the as-printed material are absent after annealing at 790°C as previously observed in L-PBF 316 L stainless steel (Voisin et al., 2021b).

After the high-temperature aging heat treatment, differences in chemical composition are observed between phases as evidenced by the STEM/HAADF image and corresponding STEM/EDS elemental maps of the annealed Ti5553 material in Fig. 11a,b. The α phase is enriched in Ti and Al while the β matrix is enriched in V, Cr, and Mo. The accompanying EDS analyses for the α and β phases are outlined in Table 1 and indicate an increase in Ti and Al concentrations of ~10 at% and ~6 at%, respectively, in the α grains compared to the surrounding matrix. The presence of residual stresses, high density of dislocations, and faint ω precipitates in the as-printed material can affect the nucleation and volume fraction of α formed during heat treatment. To verify the material is close to equilibrium after the high-temperature heat treatment, the phase diagram was calculated using CALPHAD (Fig. 11c). The calculated β-transus temperature of ≈ 830°C is close to the one reported in the literature (Kar et al., 2014; Colombo-Pulgarín et al., 2021). Estimated phase volume fractions of 68% α and 32% β at the aging treatment temperature of 600°C are in good agreement with the EBSD measurements (69% α and 31% β). Elemental compositions of α and β phases calculated by CALPHAD are reported in Table 1. Slight variations compared to our experimental measurements can be attributed to non-equilibrium conditions (i.e., longer heat treatment needed to reach thermodynamic equilibrium), EDS measurement error, and

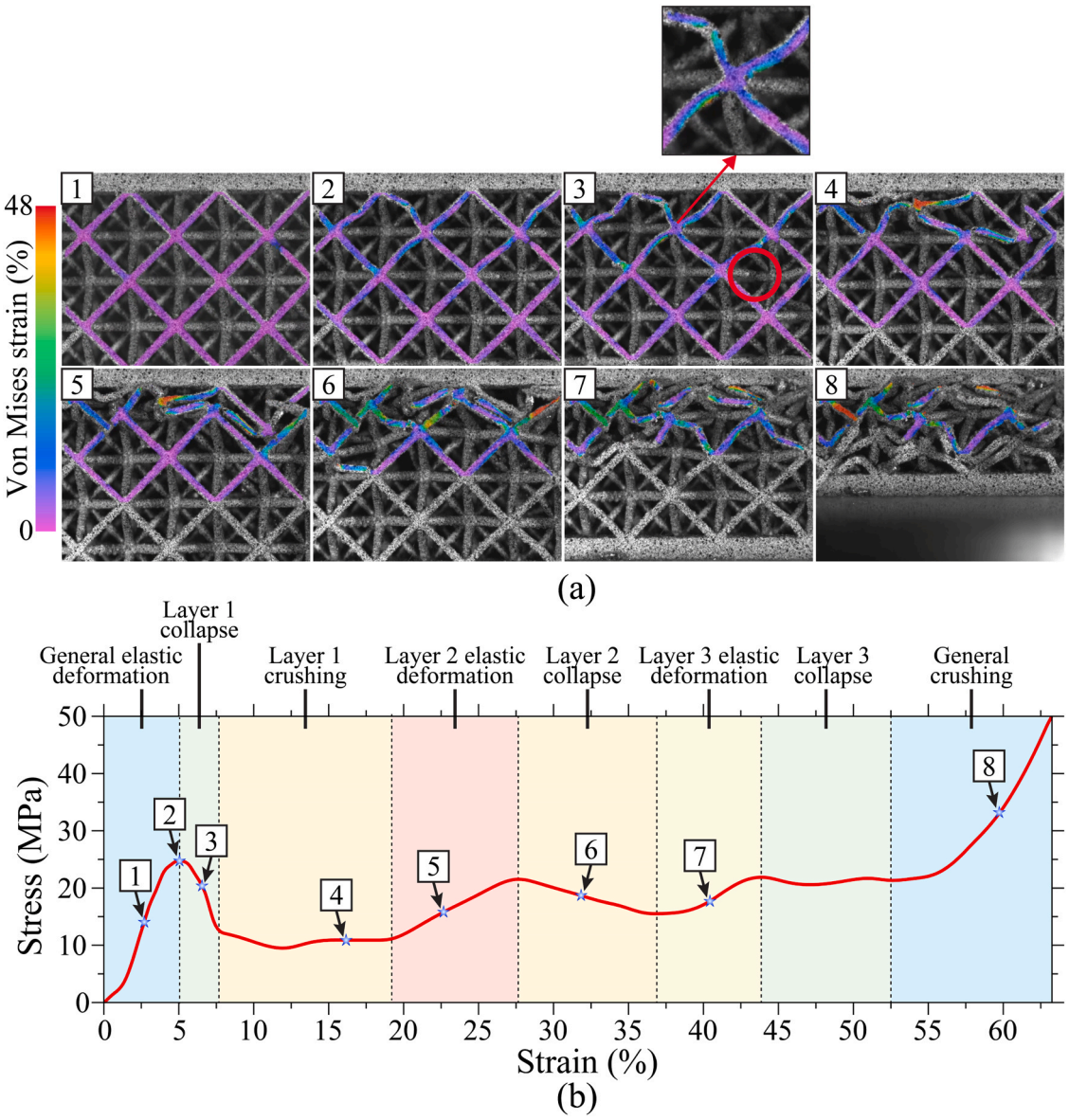

Fig. 8. : in-situ DIC compression testing of a representative lattice. (a) strain distribution maps extracted from movie 1. The red circle marks a strut loaded in tension that fractured. (b) corresponding compressive stress-strain curves. Numbers on the curve correspond to the snapshot numbers in (a).

uncertainties in assessed solubilities in the TCTI2 database; considering these uncertainties, experiments and simulations are in agreement.

In comparison to the as-built condition, once the material is solutionized at 790°C and aged at 600°C, the presence of α-phase precipitates and the reduced dislocation content increases yield strength and ultimate tensile strength to 958 ± 2 MPa and 999 ± 4 MPa, respectively, and improves the uniform elongation to ~10% (Fig. 12a). A comparison of mechanical properties among LPBF-Ti5553 as-built and after heat treatments, and conventional Ti5553 as reported in the literature is summarized in Table 2 and outlined in Fig. 12b. It should be noted that uniform elongation is a more comparable metric for ductility since samples tested in the literature possessed different initial gauge lengths. However, since UE values were not reported in (Kar et al., 2013), ETF values are listed in the present work.

4. Discussion

4.1. Bulk Ti5553: L-PBF vs. conventional

The bulk material contains features such as melt pool boundaries and columnar β grains with strong <100> texture along the build direction, indicating epitaxial growth (Vrancken et al., 2014). Additionally, the high density of dislocations likely contributes to the higher strength of the L-PBF material compared to its conventional counterpart, as shown in Fig. 12 and Table 2. Indeed, the Ti5553 bulk specimens exhibit an increase of ~100 MPa in tensile yield strength compared to the conventionally-cast material even though the L-PBF material does not contain α grains. The post-yield softening observed during uniaxial tensile loading of the as-built material has been previously reported for other titanium alloys exhibiting intense planar slip (Kumar et al., 2019; Izumi, 1986). This phenomenon has been attributed to the shearing and dissolution of coherent ω nanoprecipitates, which leads to the easy glide of trailing dislocations within the ω-free channels (Min et al., 2015; Lai et al., 2018). Thus, the presence of athermal, coherent ω nanoprecipitates in the as-built material may initiate the particle-shearing process and subsequent softening behavior leading to a ductility of about 15% ETF. Consequently, limited work hardening is observed for the as-built material as indicated by the small difference between its UTS and YS (< 100 MPa). The softening effect of ω phase and effects of pre-existing dislocations are supported by the change in mechanical

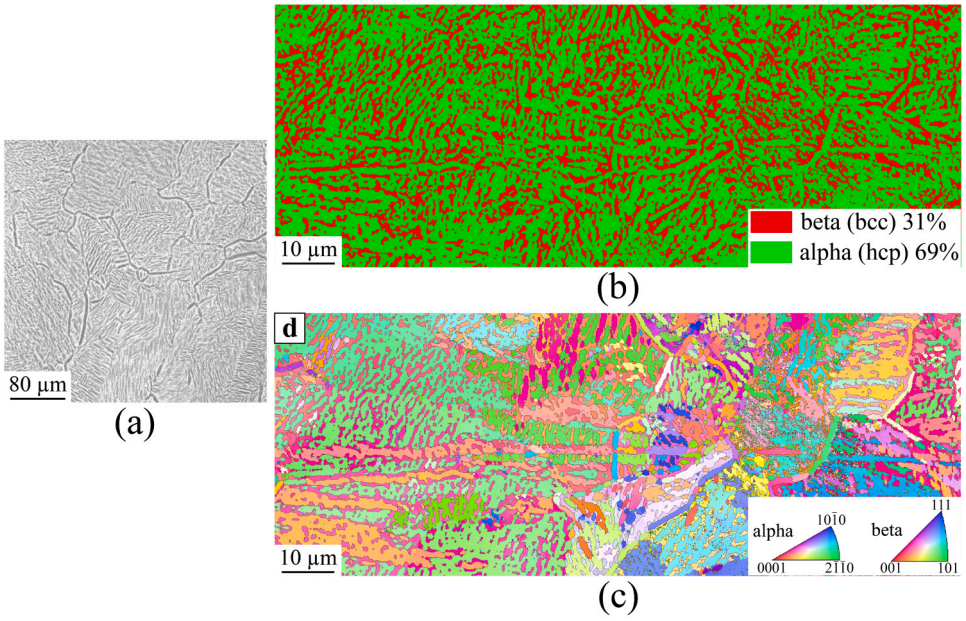

Fig. 9. : Microstructure of the bulk material annealed at 790°C (2 h) + 600°C (6 h). (a) BSE SEM image showing α (dark) and β (light) grains; (b) BF and DF TEM images highlighting α-grains or β-matrix. (c) EBSD phase map highlighting volume fractions of β and α phases of 31% and 69%, respectively; (c) EBSD IPF map.

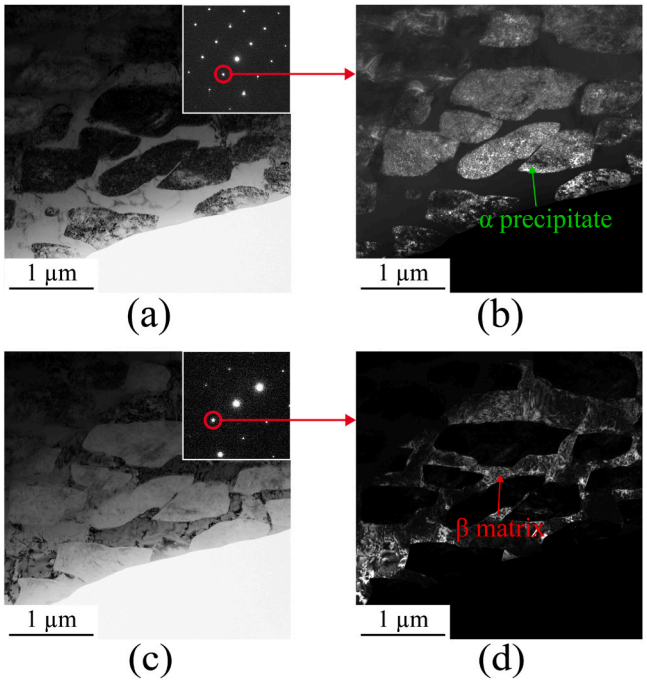

Fig. 10. : Microstructure of the bulk material annealed at 790°C (2 h) + 600°C (6 h) investigated by TEM. (a) BF and (b) DF highlighting α-grains. (c) BF and (d) DF highlighting the β-matrix with no omega phase. DF images were obtained using the corresponding diffraction spots highlighted with the red circles.

response when the material is annealed at 300°C for 1 hour. This low temperature heat treatment creates a population of β grains with numerous ω precipitates, leading to a slight decrease in yield strength by ~50 MPa compared to the as-built material and a more pronounced post-yield softening.

To strengthen and improve ductility for the as-printed material, a common industrial heat-treatment within the α+β regime was implemented. Concurrence between experimental findings and CALPHAD calculations for the relative volume fractions and phase compositions indicated that the as-printed L-PBF material responded the same as expected for conventional material after heat treatments. Prior work for improving Ti5553 strength has entailed careful control of the size, shape, and volume fraction of α grains by fine-tuning processing parameters such as aging temperature, time, and cooling rate (Panza-Giosa, 2009; Dehghan-Manshadi and Dippenaar, 2011). The α-phase interface acts as a barrier to moving dislocations and in particular, a decrease in spacing between α grains and an increase in their number density can enhance tensile yield strength due to a decrease in dislocation mean free slip path in the parent β grains (Mantri et al., 2018). As seen in the present work, annealing at 790°C + 600°C introduces a uniform distribution of α grains and removes the high density of dislocations and ω phase in the β grains, resulting in enhanced strength and uniform elongation (Fig. 4d). It should be noted the yield strength of the as-built material is only approximately 50 MPa lower than that of the annealed bulk (Fig. 12a), which demonstrates the remarkable strength of the as-built material given the absence of α grains. For the annealed material, the variation in sample-to-sample ductility could be due to remaining porosity after the heat-treatment, which has been shown to cause premature failure (Li et al., 2019; Voisin et al., 2018).

4.2. *Lattice microstructure and comparison to bulk properties*

Lattice structures provide vital weight savings for structural applications, and AM has opened a door to make more complex designs. However, AM lattices are made of thin struts or walls, which will experience different cooling rates during processing compared to bulk samples. Thus, it is important to investigate the effect on microstructures and mechanical properties. In our lattice, the ligaments possess coarse, equiaxed grains near the surface within the partially melted powder particles while the fully-melted regions in the centers of the struts contain columnar grains whose long axes are oriented towards the maximum heat flux. Similar observations were made with 316 L stainless steel ligaments <1 mm in diameter (Niendorf et al., 2014). During additive manufacturing of bulk parts, the thermal conductivity of the metal powder bed is lower than the previously solidified layer (Wauthle et al., 2015). As such, heat generally flows downward into previously solidified material, parallel to the BD. However, for sufficiently thin lattices (Britt et al., 2021), there is less surrounding dense material in

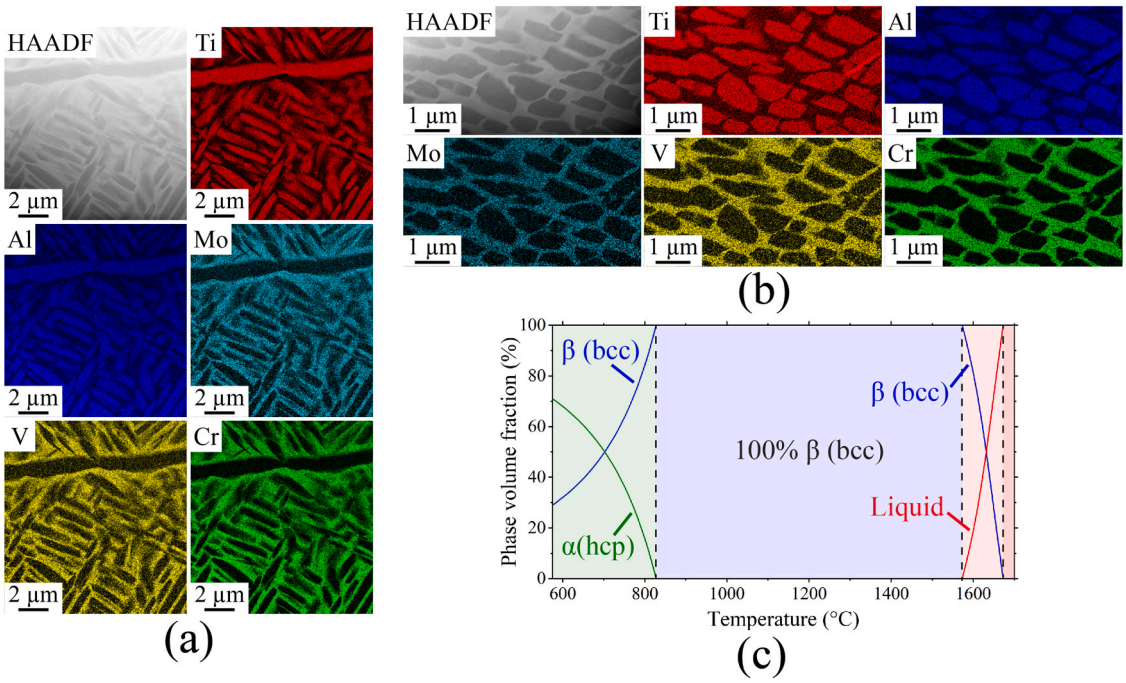

Fig. 11. : Elemental mapping by STEM/EDS of the bulk material annealed at 790°C (2 h) + 600°C (6 h) and calculated phase diagrams for Ti5553 using the TCTI2 database in combination with the Thermo-Calc 2022b software. STEM/HAADF image with corresponding STEM/EDS maps of (a) a region containing α-phase grain boundary and needle-shaped grains and (b) cross sectional view of α grains. (c) Equilibrium phase calculation highlighting the β-transus temperature at ~828°C and the phase fraction of the Liquid, β, and α phases as function of temperature (see Table 2 for phase compositions).

Table 1
Comparison between STEM/EDS and CALPHAD predictions of elemental compositions in α-phase and β-matrix, showing good agreement. Slight variations may be due to EDS measurement error, uncertainty in assessed solubilities in TCTI2 database, and non-equilibrium conditions (i.e., longer heat treatment needed to reach thermodynamic equilibrium).

Element (at%)	α			β		
	STEM/EDS		CALPHAD	STEM/EDS		CALPHAD
	Av.	stdv	Av.	Av.	stdv	Av.
Ti	85.8	0.4	87.9	76.3	1.1	68.3
Al	10.6	0.4	10.2	4.9	0.4	6.1
Mo	1.1	0.1	0.0	4.6	0.2	7.3
V	2.5	0.4	1.1	9.2	0.4	11.7
Cr	0.1	0.0	0.7	5.1	0.6	6.7

previous layers to conduct heat downward, and the heat flow will be affected by the orientation of the lattice struts. For example, Fig. 5, the direction of grain elongation aligns with BD for the 90°-oriented strut, but not for the 45°-oriented strut. In the 45°-oriented strut, the main direction of heat flow is closer to 45° (along the ligament). This is particularly visible on the pole figures where the typical grain direction of growth (<001>) is close to 45° rather than BD.

To compare the mechanical behavior between bulk and lattice struts, the Taylor Factors (TF) were calculated along the ligament direction (i.e. 90° to the BD and 45° to BD), from the IPF presented in Figs. 1 and 5, assuming uniaxial deformation (Fig. 13). According to Fig. 13a, the TF distribution does not substantially differ between the bulk (blue curve) and 90°-oriented ligament (black curve) when the load is applied perpendicular to the BD. However, when the load is applied 45° to the build direction (Fig. 13b), the bulk (green curve) shows an increase in the fraction for grains with Taylor factors over ~3 whereas the distribution of Taylor factors is broader for the 45°-oriented ligament with an average value ~2.6 (red curve). The TF predicts the yield response of individual grains due to the applied stress state and grain orientation. Moreover, "soft" or low Taylor Factor grains are favorably oriented for slip activation. Thus, solely based on average crystal orientation/texture differences, the 45°-oriented ligaments would be softer, i.e., yield at a lower stress. Accordingly, the DIC-compression results (Fig. 8) indicate plasticity would be concentrated in the 45°-oriented ligaments. This observation coincides with previous studies (Tancogne-Dejean et al., 2016; Carlton et al., 2017) on compression tested octet-truss lattices where it was observed that, upon buckling, the 45°-oriented ligaments formed "plastic hinges" followed by the subsequent "twist" or rotation of the unit cell as similarly seen at the inset of Fig. 8a(3). This failure initiation has been reported for low-density lattice structures. In summary, based on crystal orientation, as well as anticipated truss stress distributions, the lattice structure would yield at a lower applied stress than the bulk, as observed in the present study.

Although the formation of isothermal ω phase in the lattice may soften the lattice as was observed for the bulk, it may be used to nucleate refined α-precipitates which strengthens the material and opens possibilities to fine-tune the mechanical properties of L-PBF parts. Thus, their presence as well as other metastable phases in the 300°C annealed material was investigated. As seen in Fig. 9, both the nano-sized ω and α" precipitates are observed in the struts and nodes as evidenced by the extra reflections surrounding the fundamental β diffraction spots. The decomposition of the β matrix into precursory metastable phases like α'' and ω which has been widely observed in the past in both conventionally fabricated (Fan et al., 2017; Sabol et al., 2014) and electron beam welded AM material (Marvel et al., 2017; Zhang et al., 2022). While orthorhombic α'' has a lower lattice distortion with respect to the β matrix (Shariff et al., 2011; Cardoso et al., 2014), and therefore a negligible role in hardening, its role alongside ω in the nucleation of the α phase upon further heat treatment (Zheng et al., 2016c, 2016d) has sparked efforts to control aging conditions in order to refine the size, morphology and distribution of the strengthening α particles. In particular, intermediate aging at 350°C has been shown to precipitate the ω and α" phases which subsequently generates compositional and stress variations within the β matrix (Nag et al., 2009; Shi et al., 2019); upon further aging at higher temperatures (>500°C), these "compositional pockets" (Zheng et al., 2016a) associated with the nano-sized

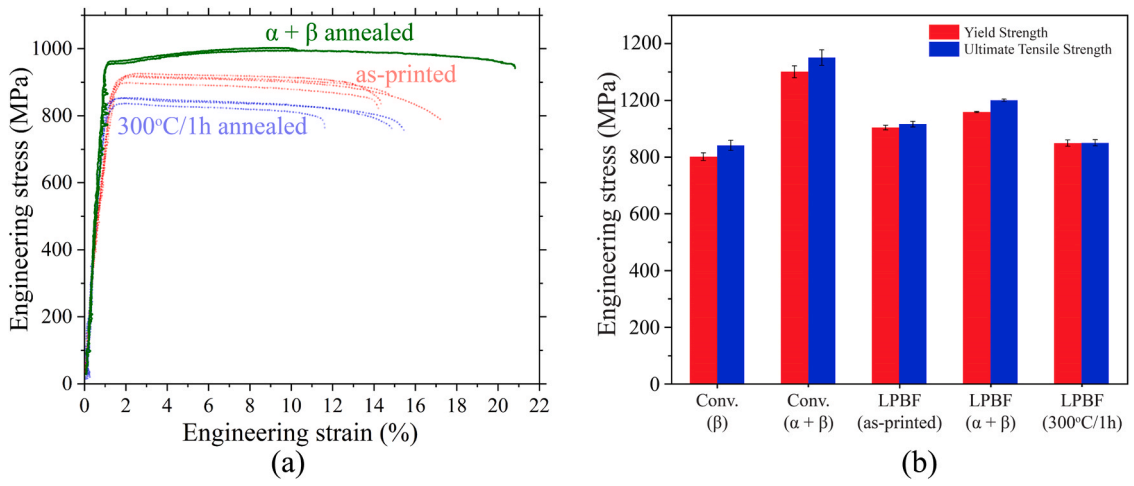

Fig. 12. : Tensile properties of bulk material annealed at 790°C (2 h) + 600°C (6 h). (a) Engineering stress-strain curves compared to the as-printed and 300°C/1 h annealed materials. (b) Mechanical strength summary including literature data on the conventional Ti5553 (β and α + β annealed conditions) (Kar et al., 2013).

Table 2
Comparison of mechanical properties between our bulk SLM-280 Ti5553 and values reported in the literature for conventional β and α + β Ti5553.

Condition	Yield Strength (MPa)	UTS (MPa)	Engineering UE (%)	ETF (%)	Authors
Conventional β Ti5553	636 ± 25	-	-	13 ± 2	(Shekhar et al., 2015)
	782	810	<1%	5	(Panza-Giosa, 2009)[a]
	800	840	-	12	(Sadeghpour et al., 2017)
	461	794	~15%	32	(Banoth et al., 2015)
SLM Ti5553 as-built	903 ± 8	915 ± 10	<3%	15 ± 1	*Present study*
Conventional α + β annealed	1100	1150	-	8	(Sadeghpour et al., 2017)[b]
SLM α + β annealed	958 ± 2	999 ± 4	<10%	16 ± 6	*Present study*[b]
SLM 300°C annealed	848 ± 11	849 ± 11	<1%	19 ± 2	*Present study*

[a] ω phase present
[b] ~800°C + 600°C

precipitates act as nucleation sites for a high number density of refined α precipitates (Settefrati et al., 2011; Coakley et al., 2015). Thus, while the ω phase has proven in some cases to be deleterious to mechanical properties depending on its volume fraction (Williams et al., 1971), size, and morphology (Gao et al., 2019), it can optimize material strength when used as a precursor for α phase nucleation upon optimized heat treatments. Thus, the present study sets the stage for future work to compare the performance of lattice parts annealed into the α/β regime with and without an intermediate ~300°C aging step.

In addition to the above findings, we determined the failure mode for the Ti5553 octet lattice is similar to that of octet 316 L stainless steel and Ti64 lattices, i.e. failure initiates at specimen boundaries or the boundaries between regions with lattice geometry and side walls with thickness approximating bulk material. This initial failure is followed by a layer-by-layer collapse which is reflected as oscillations in the stress-strain curves. Indeed, Dejean et al (Tancogne-Dejean et al., 2016). evaluated the mechanical response of a low-density L-PBF 316 L stainless steel lattice in uniaxial compression and also observed localized crushing, while other studies (Ruiz de Galarreta et al., 2021) (Carlton et al., 2022) have examined the role of introduced defects such as graded density in Ti64 lattices and discovered deformation confined to the sample boundaries. This implies specimen topology and surface roughness may play dominant roles in the lattice deformation behavior.

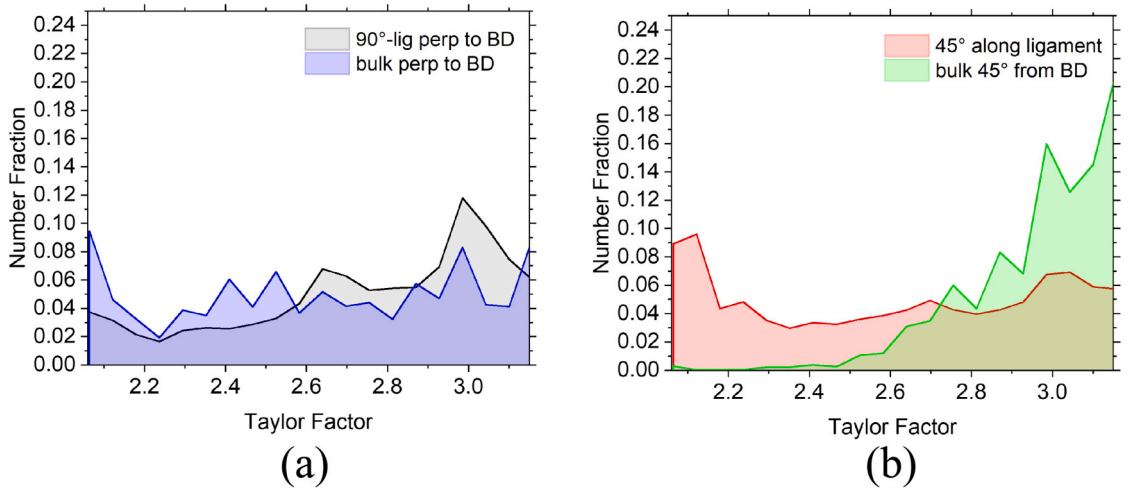

Fig. 13. : Taylor factors (TF) for bulk and lattice Ti5553. TF distributions for **(a)** bulk vs. 90°-oriented ligament when the load is applied perpendicular to BD and **(b)** bulk vs. 45°-oriented ligament when the load is applied at 45° from BD.

Nonetheless, it should be noted that the Ti5553 lattice still displays a higher specific yield strength (~54 MPa/(g·cm^3)) compared to the 316 L stainless steel octet truss (~25 MPa/g·cm^3)) examined in the previous work (Tancogne-Dejean et al., 2016), and to the electron beam melted Ti-14Mo octet truss (~43 MPa/g·cm^3) subjected to isothermal omega annealing by Duport et al. [87]. As seen in Fig. S4 (Supplementary Information), although the Ti-14Mo lattice demonstrates a "smoother" post-yield response and less dramatic variations in stress amplitude – features the authors ascribed to the TWIP effect and large work-hardening rate (WHR) uniquely observed for the bulk counterpart - the energy efficiency of the Ti5553 lattice (69.3%) is similar to that of Ti-14Mo (63.9%) despite the Ti5553 bulk demonstrating a low work-hardening capacity. Additionally, the volumetric energy absorption (obtained by integrating area under the curve until densification) for our Ti5553 lattice is 11.5 mJ/mm^3 compared to 10.5 mJ/mm^3 for the omega-annealed Ti-14Mo. Thus, using bulk WHR to predict lattice mechanical performance, in particular the resistance of constituent struts to buckling, does not apply. Instead, the post-yielding behavior and corresponding energy absorption properties of lattices are more likely dictated by microstructural differences achieved by laser powder bed fusion, making L-PBF Ti5553 a model material candidate for lightweight structural applications. Future improvements to Ti5553 lattice mechanical performance can include increasing strut diameter (Alghamdi et al., 2020) (balanced with weight savings) in addition to modifying single strut microstructure via post-process annealing to introduce the aforementioned hard, second-phase precipitates which strengthen the lattice's mechanical response to uniaxial compression.

As demonstrated by their respective Taylor factors, the contrasting mechanical response between the bulk and lattice indicates the challenges in extrapolating lattice mechanical performance based on bulk properties, especially given their different processing conditions and resulting microstructures. In addition, low temperature annealing for the residual stress relaxation can cause minor phase nucleation that can be detrimental to the mechanical properties.

5. Conclusions

The present study has investigated the multi-length microstructures and mechanical properties of L-PBF Ti5553 bulk and lattice parts. The comprehensive characterization of Ti5553 in the as-printed and annealed conditions guides post-processing L-PBF Ti5553 and can be used as a benchmark to aid in the design and optimization of L-PBF materials. The following insights were gathered:

- The as-printed bulk material contains a high density of dislocations, which makes its strength ~100 MPa greater than conventional β-Ti5553 with similar microstructure and comparable to annealed/dual-phase α + β Ti5553. Despite the absence of cellular structures, the homogeneous distribution of dislocations improved material yield strength and the present processing parameters can be refined and further applied to all L-PBF materials.
- The 300°C-annealed bulk and lattice materials contain coarser ω precipitates, which are near absent in the as-printed material. This leads to a decrease in yield strength after annealing. This highlights the need to carefully design stress relief heat treatments for LPBF Ti-alloys. Temperatures above 500 °C will nucleate α phase but temperatures around 300 °C and below will nucleate or coarsen the existing ω precipitates in the β phase. The repercussions on mechanical properties will be different.
- Compared to LPBF bulk material, lattice parts have different microstructures. This is especially true for 45º-oriented ligaments for which the direction of the thermal gradient upon solidification no longer aligns with the build direction. This leads to smaller average grain sizes, higher fraction of high-angle grain boundaries, and a different texture leading to different Taylor factor distributions. These differences suggest an onset of plasticity in the lattice parts at a lower stress compared to bulk material. It is important to note that because of these differences, lattice properties cannot simply be extrapolated from bulk properties.
- The introduction of hard phases such as α via heat treatments is one route to enhance the strength of Ti5553 L-PBF parts. α grains are known to nucleate on ω precipitates when available. The presence of very fine isothermal ω precipitates after LPBF can provide an alternative pathway to controlling the size and distribution of the α phase in rapidly solidified Ti alloys.

CRediT authorship contribution statement

Margaret Wu: Conceptualization, Data curation, Formal analysis, Investigation, Methodology, Writing – original draft, Writing – review & editing. **Marissa Linne:** Data curation, Formal analysis, Investigation, Validation, Writing – original draft, Writing – review & editing. **Jean-Baptiste Forien:** Data curation, Formal analysis, Investigation, Writing – original draft. **Nathan R. Barton:** Formal analysis, Funding acquisition, Validation, Writing – original draft. **Jianchao Ye:** Data curation, Formal analysis, Investigation. **Kavan Hazeli:** Conceptualization, Formal analysis, Investigation, Methodology, Writing – original draft. **Aurelien Perron:** Data curation, Formal analysis, Investigation, Methodology, Validation, Writing – original draft. **Kaila Bertsch:** Data curation, Formal analysis, Validation, Visualization, Writing – original draft. **Y. Morris Wang:** Conceptualization, Data curation, Investigation, Writing – original draft. **Thomas Voisin:** Conceptualization, Data curation, Formal analysis, Funding acquisition, Investigation, Methodology, Project administration, Resources, Supervision, Validation, Visualization, Writing – original draft, Writing – review & editing.

Declaration of Competing Interest

The authors declare that they have no known competing financial interests or personal relationships that could have appeared to influence the work reported in this paper.

Acknowledgements

This work was performed under the auspices of the US Department of Energy by Lawrence Livermore National Laboratory under contract No. DE-AC52-07NA27344. This research used resources of the Advanced Light Source, which is a DOE Office of Science User Facility under contract no. DE-AC02-05CH11231. K. Hazeli effort was supported by the Mechanics of Materials and Structures (MOMS), USA program at the National Science Foundation (NSF), USA under Award Number: 1943465.

Appendix A. Supporting information

Supplementary data associated with this article can be found in the online version at doi:10.1016/j.jmatprotec.2024.118354.

References

Agarwal, N., Bhattacharjee, A., Ghosal, P., Nandy, T., Sagar, P., 2008. Heat treatment, microstructure, and mechanical properties of a metastable β titanium alloy timetal® 21. Trans. Indian Inst. Met. 61.

Alam, T., 2014. On the Role of C Addition on Precipitation in a beta-Titanium Alloy. Metall. Mat. Trans. A 45A, 1089–1095.

Alghamdi, A., Maconachie, T., Downing, D., Brandt, M., Qian, M., Leary, M., 2020. Effect of additive manufactured lattice defects on mechanical properties: an automated method for the enhancement of lattice geometry. Int. J. Adv. Manuf. Technol. 108 (3), 957–971.

Alphy, G., Sharma, V., Divakar, R., Sabeena, M., Mohandas, E., 2017. Transmission electron microscopy studies and modeling of 3D reciprocal space of omega forming alloy. Micron 102, 73–87.

Babamiri, B.B., Mayeur, J.R., Hazeli, K., 2022. Synchronous involvement of topology and microstructure to design additively manufactured lattice structures. Addit. Manuf. 52.

Bakhshivash, S., Asgari, H., Russo, P., Dibia, C.F., Ansari, M., Gerlich, A.P., Toyserkani, E., 2019. Printability and microstructural evolution of Ti-5553 alloy fabricated by modulated laser powder bed fusion. Int. J. Adv. Manuf. Technol. 103 (9), 4399–4409.
Banerjee, D., Williams, J.C., 2013. Perspectives on titanium science and technology. Acta Mater. 61 (3), 844–879.
Banoth, R., Sarkar, R., Bhattacharjee, A., Nandy, T.K., Nageswara Rao, G.V.S., 2015. Effect of boron and carbon addition on microstructure and mechanical properties of metastable beta titanium alloys. Mater. Des. 67, 50–63.
Bertsch, K.M., Meric de Bellefon, G., Kuehl, B., Thoma, D.J., 2020. Origin of dislocation structures in an additively manufactured austenitic stainless steel 316L. Acta Mater. 199, 19–33.
Britt, C., Montgomery, C.J., Brand, M.J., Liu, Z.-K., Carpenter, J.S., Beese, A.M., 2021. Effect of processing parameters and strut dimensions on the microstructures and hardness of stainless steel 316L lattice-emulating structures made by powder bed fusion. Addit. Manuf. 40.
Cardoso, F.F., Ferrandini, P.L., Lopes, E.S.N., Cremasco, A., Caram, R., 2014. Ti-Mo alloys employed as biomaterials: effects of composition and aging heat treatment on microstructure and mechanical behavior. J. Mech. Behav. Biomed. Mater. 32, 31–38.
Carlton, H.D., Klein, K.D., Elmer, J.W., 2019. Evolution of microstructure and mechanical properties of selective laser melted Ti-5Al-5V–5Mo-3Cr after heat treatments. Sci. Technol. Weld. Join. 24 (5), 465–473.
Carlton, H.D., Lind, J., Messner, M.C., Volkoff-Shoemaker, N.A., Barnard, H.S., Barton, N. R., Kumar, M., 2017. Mapping local deformation behavior in single cell metal lattice structures. Acta Mater. 129, 239–250.
Carlton, H.D., Volkoff-Shoemaker, N.A., Messner, M.C., Barton, N.R., Kumar, M., 2022. Incorporating defects into model predictions of metal lattice-structured materials. J. Mater. Sci. Eng. A 832.
Champley, K.M., Willey, T.M., Kim, H., Bond, K., Glenn, S.M., Smith, J.A., Kallman, J.S., Brown, W.D., Seetho, I.M., Keene, L., Azevedo, S.G., McMichael, L.D., Overturf, G., Martz, H.E., 2022. Livermore tomography tools: Accurate, fast, and flexible software for tomographic science. NDT E Int. 126, 102595.
Clement, N., Lenain, A., Jacques, P.J., 2007. Mechanical Property Optimization via Microstructural Control of New Metastable Beta Titanium Alloys. JOM 59, 50–53.
Coakley, J., Vorontsov, V.A., Jones, N.G., Radecka, A., Bagot, P.A.J., Littrell, K.C., Heenan, R.K., Hu, F., Magyar, A.P., Bell, D.C., Dye, D., 2015. Precipitation processes in the Beta-Titanium alloy Ti–5Al–5Mo–5V–3Cr. J. Alloy. Compd. 646, 946–953.
Colombo-Pulgarín, J.C., Biffi, C.A., Vedani, M., Celentano, D., Sánchez-Egea, A., Boccardo, A.D., Ponthot, J.P., 2021. Beta titanium alloys processed by laser powder bed fusion: a review. J. Mater. Eng. Perform. 30 (9), 6365–6388.
Cotton, J.D., Briggs, R.D., Boyer, R.R., Tamirisakandala, S., Russo, P., Shchetnikov, N., Fanning, J.C., 2015. State of the art in beta titanium alloys for airframe applications. JOM 67 (6), 1281–1303.
D. V, F. N, A. M, 2001. Effective properties of the octet-truss lattice material. J. Mech. Phys. Solids 49, 1747–1769.
DebRoy, T., Wei, H.L., Zuback, J.S., Mukherjee, T., Elmer, J.W., Milewski, J.O., Beese, A. M., Wilson-Heid, A., De, A., Zhang, W., 2018. Additive manufacturing of metallic components – process, structure and properties. Prog. Mater. Sci. 92, 112–224.
Dehghan-Manshadi, A., Dippenaar, R.J., 2011. Development of α-phase morphologies during low temperature isothermal heat treatment of a Ti–5Al–5Mo–5V–3Cr alloy. J. Mater. Sci. Eng. A 528 (3), 1833–1839.
Fan, J., Li, J., Zhang, Y., Kou, H., Ghanbaja, J., Gan, W., Germain, L., Esling, C., 2017. The origin of striation in the metastable beta phase of titanium alloys observed by transmission electron microscopy. J. Appl. Crystallogr 50 (Pt 3), 795–804.
Gao, J., Knowles, A.J., Guan, D., Rainforth, W.M., 2019. ω phase strengthened 1.2GPa metastable β titanium alloy with high ductility. Scr. Mater. 162, 77–81.
Ghosh, A., Sivaprasad, S., Bhattacharjee, A., Kar, S.K., 2013. Microstructure–fracture toughness correlation in an aircraft structural component alloy Ti–5Al–5V–5Mo–3Cr. J. Mater. Sci. Eng. A 568, 61–67.
Hazeli, K., Babamiri, B.B., Indeck, J., Minor, A., Askari, H., 2019. Microstructure-topology relationship effects on the quasi-static and dynamic behavior of additively manufactured lattice structures. Mater. Des. 176.
Hazeli, K., June, D., Anantwar, P., Babamiri, B.B., 2022. Mechanical behavior of additively manufactured GRCop-84 copper alloy lattice structures. Addit. Manuf. 56.
Hernandez, J., Li, S.J., Martinez, E., Murr, L.E., Pan, X.M., Amato, K.N., Cheng, X.Y., Yang, F., Terrazas, C.A., Gaytan, S.M., Hao, Y.L., Yang, R., Medina, F., Wicker, R.B., 2013. Microstructures and hardness properties for β-phase Ti–24Nb–4Zr–7.9Sn alloy fabricated by electron beam melting. J. Mater. Sci. Technol. 29 (11), 1011–1017.
Huang, H.-l, Li, D., Chen, C., Li, R.-d, Zhang, X.-y, Liu, S.-c, Zhou, K.-c, 2021. Selective laser melted near-beta titanium alloy Ti-5Al-5Mo-5V–1Cr-1Fe: Microstructure and mechanical properties. J. Cent. South Univ. 28 (6), 1601–1614.
S.Ha.O. Izumi, Correlation of Tensile Properties, Deformation Modes, and Phase Stability in Commercial/3-Phase Titanium Alloys, Metallurgical Transactions A (1986).
Jones, N.G., Dashwood, R.J., Jackson, M., Dye, D., 2009. β Phase decomposition in Ti–5Al–5Mo–5V–3Cr. Acta Mater. 57 (13), 3830–3839.
Kar, S.K., Ghosh, A., Fulzele, N., Bhattacharjee, A., 2013. Quantitative microstructural characterization of a near beta Ti alloy, Ti-5553 under different processing conditions. Mater. Charact. 81, 37–48.
Kar, S.K., Suman, S., Shivaprasad, S., Chaudhuri, A., Bhattacharjee, A., 2014. Processing-microstructure-yield strength correlation in a near β Ti alloy, Ti–5Al–5Mo–5V–3Cr. J. Mater. Sci. Eng. A 610, 171–180.
Kaufman, L., Bernstein, H., 1970. Computer calculation of phase diagrams with special reference to refractory metals. Academic Press Inc, United States.
Kumar, S.S.S., Pavithra, B., Singh, V., Ghosal, P., Raghu, T., 2019. Tensile anisotropy associated microstructural and microtextural evolution in a metastable beta titanium alloy. J. Mater. Sci. Eng. A 747, 1–16.
Lai, M.J., Li, T., Raabe, D., 2018. ω phase acts as a switch between dislocation channeling and joint twinning- and transformation-induced plasticity in a metastable β titanium alloy. Acta Mater. 151, 67–77.
Liu, C.M., Wang, H.M., Tian, X.J., Liu, D., 2014. Development of a pre-heat treatment for obtaining discontinuous grain boundary α in laser melting deposited Ti–5Al–5Mo–5V–1Cr–1Fe alloy. J. Mater. Sci. Eng. A 604, 176–182.
Liu, Y.J., Zhang, Y.S., Zhang, L.C., 2019. Transformation-induced plasticity and high strength in beta titanium alloy manufactured by selective laser melting. Materialia 6.
Li, Z., Voisin, T., McKeown, J.T., Ye, J., Braun, T., Kamath, C., King, W.E., Wang, Y.M., 2019. Tensile properties, strain rate sensitivity, and activation volume of additively manufactured 316L stainless steels. Int. J. Plast. 120, 395–410.
Lütjering, G., Albrecht, J., Sauer, C., Krull, T., 2007. The influence of soft, precipitate-free zones at grain boundaries in Ti and Al alloys on their fatigue and fracture behavior. J. Mater. Sci. Eng. A 468-470, 201–209.
MacDowell, A., Parkinson, D., Haboub, A., Schaible, E., Nasiatka, J., Yee, C., Jameson, J., Ajo-Franklin, J., Brodersen, C., McElrone, A., 2012. X-ray micro-tomography at the Advanced Light Source. Developments in X-Ray Tomography VIII. SPIE,, pp. 298–311.
Mantri, S.A., Choudhuri, D., Alam, T., Viswanathan, G.B., Sosa, J.M., Fraser, H.L., Banerjee, R., 2018. Tuning the scale of α precipitates in β-titanium alloys for achieving high strength. Scr. Mater. 154, 139–144.
Marvel, C.J., Sabol, J.C., Pasang, T., Watanabe, M., Misiolek, W.Z., 2017. Improving the mechanical properties of the fusion zone in electron-beam welded Ti-5Al-5Mo-5V–3Cr alloys. Metall. Mat. Trans. A 48 (4), 1921–1930.
Min, X., Emura, S., Zhang, L., Tsuzaki, K., Tsuchiya, K., 2015. Improvement of strength–ductility tradeoff in β titanium alloy through pre-strain induced twins combined with brittle ω phase. J. Mater. Sci. Eng. A 646, 279–287.
Nag, S., Banerjee, R., Srinivasan, R., Hwang, J.Y., Harper, M., Fraser, H.L., 2009. ω-Assisted nucleation and growth of α precipitates in the Ti–5Al–5Mo–5V–3Cr–0.5Fe β titanium alloy. Acta Mater. 57 (7), 2136–2147.
Niendorf, T., Brenne, F., Schaper, M., 2014. Lattice structures manufactured by SLM: on the effect of geometrical dimensions on microstructure evolution during processing. Metall. Mater. Trans. B 45 (4), 1181–1185.
Paiotti Marcondes Guimarães, R., Callegari, B., Warchomicka, F., Aristizabal, K., Soldera, F., Mücklich, F., Cavalcanti Pinto, H., 2020. In situ analysis of the phase transformation kinetics in the β-water-quenched Ti-5Al-5Mo-5V–3Cr-1Zr alloy during ageing after fast heating. Quantum Beam Sci. 4 (1).
Panza-Giosa, R., 2009. The effect of heat treatment on the microstructure evolution and mechanical properties of Ti-5Al-5V–5Mo-3Cr, and its potential applications in landing gears Dept. of Materials Science and Engineering. McMaster University.
Ramachandiran, N., Asgari, H., Dibia, F., Eybel, R., Keshavarzkermani, A., Gerlich, A., Toyserkani, E., 2023. Anisotropic tensile behavior of laser powder-bed fusion made Ti5553 parts. J. Mater. Sci. Eng. A 865, 144633.
Ruiz de Galarreta, S., Doyle, R.J., Jeffers, J., Ghouse, S., 2021. Laser powder bed fusion of porous graded structures: a comparison between computational and experimental analysis. J. Mech. Behav. Biomed. Mater. 123, 104784.
Sabol, J.C., Marvel, C.J., Watanabe, M., Pasang, T., Misiolek, W.Z., 2014. Confirmation of the ω-phase in electron beam welded Ti–5Al–5V–5Mo–3Cr by high-resolution scanning transmission electron microscopy: An initial investigation into its effects on embrittlement. Scr. Mater. 92, 15–18.
Sadeghpour, S., Abbasi, S.M., Morakabati, M., Bruschi, S., 2017. Correlation between alpha phase morphology and tensile properties of a new beta titanium alloy. Mater. Des. 121, 24–35.
Saunders N, M.A., 1998. CALPHAD, calculation of phase diagrams, a comprehensive guide. Pergamon Press, Oxford.
Schwab, H., Bönisch, M., Giebeler, L., Gustmann, T., Eckert, J., Kühn, U., 2017. Processing of Ti-5553 with improved mechanical properties via an in-situ heat treatment combining selective laser melting and substrate plate heating. Mater. Des. 130, 83–89.
Schwab, H., Palm, F., Kühn, U., Eckert, J., 2016. Microstructure and mechanical properties of the near-beta titanium alloy Ti-5553 processed by selective laser melting. Mater. Des. 105, 75–80.
Settefrati, A., Aeby-Gautier, E., Appolaire, B., Dehmas, M., Geandier, G., Khelifati, G., 2013. Low Temperature Transformations in β-Metastable Ti 5553 Titanium Alloy. Mater. Sci. Forum 738-739, 97–102.
Settefrati, A., et al., 2011. Precipitation in a near Beta Titanium Alloy on Ageing: Influence of Heating Rate and Chemical Composition of the Beta-Metastable Phase. Solid State Phenom. 172-174.
Shariff, T., Cao, X., Chromik, R.R., Wanjara, P., Cuddy, J., Birur, A., 2011. Effect of joint gap on the quality of laser beam welded near-β Ti-5553 alloy with the addition of Ti–6Al–4V filler wire. J. Mater. Sci. 47 (2), 866–875.
Sharma, D., Kada, S.R., Fabijanic, D., Parfitt, D., Chen, B., Roebuck, B., Fitzpatrick, M.E., Barnett, M.R., 2021. The ageing response of direct laser deposited metastable β-Ti alloy, Ti–5Al–5Mo–5V–3Cr. Addit. Manuf. 48.
Shekhar, S., Sarkar, R., Kar, S.K., Bhattacharjee, A., 2015. Effect of solution treatment and aging on microstructure and tensile properties of high strength β titanium alloy, Ti–5Al–5V–5Mo–3Cr. Mater. Des. 66, 596–610.
Shi, R., Zheng, Y., Banerjee, R., Fraser, H.L., Wang, Y., 2019. ω-Assisted α nucleation in a metastable β titanium alloy. Scr. Mater. 171, 62–66.
Song, B., Chen, Y., Xiao, W., Zhou, L., Ma, C., 2020. Formation of intermediate phases and their influences on the microstructure of high strength near-β titanium alloy. J. Mater. Sci. Eng. A 793.
Tancogne-Dejean, T., Spierings, A.B., Mohr, D., 2016. Additively-manufactured metallic micro-lattice materials for high specific energy absorption under static and dynamic loading. Acta Mater. 116, 14–28.

Voisin, T., Calta, N.P., Khairallah, S.A., Forien, J.-B., Balogh, L., Cunningham, R.W., Rollett, A.D., Wang, Y.M., 2018. Defects-dictated tensile properties of selective laser melted Ti-6Al-4V. Mater. Des. 158, 113–126.
Voisin, T., Forien, J.-B., Perron, A., Aubry, S., Bertin, N., Samanta, A., Baker, A., Wang, Y. M., 2021a. New insights on cellular structures strengthening mechanisms and thermal stability of an austenitic stainless steel fabricated by laser powder-bed-fusion. Acta Mater. 203, 116476.
Voisin, T., Forien, J.-B., Perron, A., Aubry, S., Bertin, N., Samanta, A., Baker, A., Wang, Y. M., 2021b. New insights on cellular structures strengthening mechanisms and thermal stability of an austenitic stainless steel fabricated by laser powder-bed-fusion. Acta Mater. 203.
Vrancken, B., Thijs, L., Kruth, J.P., Van Humbeeck, J., 2014. Microstructure and mechanical properties of a novel β titanium metallic composite by selective laser melting. Acta Mater. 68, 150–158.
Wain, N., Hao, X.J., Ravi, G.A., Wu, X., 2010. The influence of carbon on precipitation of α in Ti–5Al–5Mo–5V–3Cr. J. Mater. Sci. Eng. A 527 (29-30), 7673–7683.
Wang, Y.M., Voisin, T., McKeown, J.T., Ye, J., Calta, N.P., Li, Z., Zeng, Z., Zhang, Y., Chen, W., Roehling, T.T., Ott, R.T., Santala, M.K., Depond, P.J., Matthews, M.J., Hamza, A.V., Zhu, T., 2018. Additively manufactured hierarchical stainless steels with high strength and ductility. Nat. Mater. 17 (1), 63–71.
Wauthle, R., Vrancken, B., Beynaerts, B., Jorissen, K., Schrooten, J., Kruth, J.-P., Van, J., 2015. Humbeeck, Effects of build orientation and heat treatment on the microstructure and mechanical properties of selective laser melted Ti6Al4V lattice structures. Addit. Manuf. 5, 77–84.
Williams, J.C., de Fontaine, D., Paton, N.E., 1973. The omega-phase as an example of an unusual shear transformation. Metall. Trans. 4, 2701–2708.
Williams, J.C., Hickman, B.S., Marcus, H.L., 1971. The effect of omega phase on the mechanical properties of titanium alloys. Metall. Trans. 2, 1913–1919.
Yang, P., Johnson, K.L., Carroll, J.D., Buckner, J.L., Blea-Kirby, M.A., Groves, C., Coker, E.N., 2023. Thermophysical properties of additively manufactured Ti-5553 alloy. Addit. Manuf. 76, 103769.
Zafari, A., Lui, E.W., Jin, S., Li, M., Molla, T.T., Sha, G., Xia, K., 2020. Hybridisation of microstructures from three classes of titanium alloys. J. Mater. Sci. Eng. A 788.
Zafari, A., Xia, K., 2019. Superior titanium from hybridised microstructures – A new strategy for future alloys. Scr. Mater. 173, 61–65.
Zhang, R., Ma, Y., Qi, M., Huang, S., Youssef, S.S., Xi, G., Qiu, J., Lei, J., Yang, R., Wang, P., 2022. The effect of precursory α and ω phase on microstructure evolution and tensile properties of metastable β titanium alloy. J. Mater. Res. Technol. 16, 912–921.
Zhang, H., Wang, C., Zhang, S., Zhou, G., Chen, L., 2018. Evolution of Secondary alpha Phase during Aging Treatment in Novel near beta Ti-6Mo-^{5}V–^{3}Al-2Fe Alloy. Materials 11 (11).
Zheng, Y., Williams, R.E.A., Nag, S., Banerjee, R., Fraser, H.L., Banerjee, D., 2016b. The effect of alloy composition on instabilities in the β phase of titanium alloys. Scr. Mater. 116, 49–52.
Zheng, Y., Williams, R.E.A., Sosa, J.M., Alam, T., Wang, Y., Banerjee, R., Fraser, H.L., 2016a. The indirect influence of the ω phase on the degree of refinement of distributions of the α phase in metastable β-Titanium alloys. Acta Mater. 103, 165–173.
Zheng, Y., Williams, R.E.A., Sosa, J.M., Wang, Y., Banerjee, R., Fraser, H.L., 2016d. The role of the ω phase on the non-classical precipitation of the α phase in metastable β-titanium alloys. Scr. Mater. 111, 81–84.
Zheng, Y., Williams, R.E.A., Wang, D., Shi, R., Nag, S., Kami, P., Sosa, J.M., Banerjee, R., Wang, Y., Fraser, H.L., 2016c. Role of ω phase in the formation of extremely refined intragranular α precipitates in metastable β-titanium alloys. Acta Mater. 103, 850–858.
Zhong, Y., Liu, L., Wikman, S., Cui, D., Shen, Z., 2016. Intragranular cellular segregation network structure strengthening 316L stainless steel prepared by selective laser melting. J. Nucl. Mater. 470, 170–178.